Journal Pre-proof

N-doped hard/soft double-carbon-coated $Na_3V_2(PO_4)_3$ hybrid-porous microspheres with pseudocapacitive behaviour for ultrahigh power sodium-ion batteries

Ke Sun, Yuebo Hu, Xudong Zhang, Kwan San Hui, Keliang Zhang, Guogang Xu, Jingyun Ma, Wen He

Please cite this article as: K. Sun, Y. Hu, X. Zhang, K. San Hui, K. Zhang, G. Xu, J. Ma, W. He, N-doped hard/soft double-carbon-coated $Na_3V_2(PO_4)_3$ hybrid-porous microspheres with pseudocapacitive behaviour for ultrahigh power sodium-ion batteries, *Electrochimica Acta* (2020), doi: https://doi.org/10.1016/j.electacta.2020.135680.

This is a PDF file of an article that has undergone enhancements after acceptance, such as the addition of a cover page and metadata, and formatting for readability, but it is not yet the definitive version of record. This version will undergo additional copyediting, typesetting and review before it is published in its final form, but we are providing this version to give early visibility of the article. Please note that, during the production process, errors may be discovered which could affect the content, and all legal disclaimers that apply to the journal pertain.
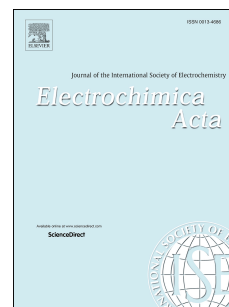
Sample CRediT author statement

Xudong Zhang and **Kwan San Hui**: Project administration, Conceptualization and Methodology.

Yuebo Hu: Software Data curation, Writing-Original draft preparation.

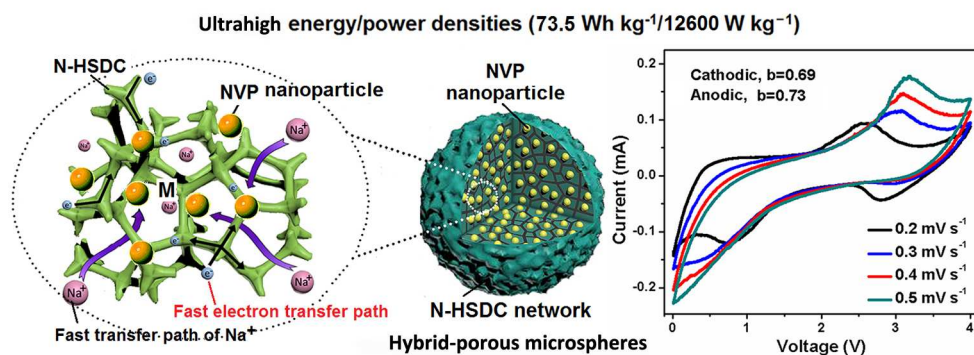**Ke Sun**: Writing, Formal analysis and Investigation.

Keliang Zhang: Visualization, Investigation and Data Curation.

Guogang Xu: Software, Validation.

Jingyun Ma: Resources and administration.

Wen He: Supervision, Writing- Reviewing and Editing.

Graphical abstract

Ultrahigh energy/power densities (73.5 Wh kg^{-1}/12600 W kg^{-1})

N-doped hard/soft double-carbon-coated $Na_3V_2(PO_4)_3$ hybrid-porous microspheres with pseudocapacitive behaviour for ultrahigh power sodium-ion batteries

Ke Sun[a], Yuebo Hu[a], Xudong Zhang [a,*], Kwan San Hui[c,*], Keliang Zhang[a], Guogang Xu[b], Jingyun Ma[a] & Wen He [a,*]

[a]College of Material Science and Engineering, Qilu University of Technology (Shandong Academy of Sciences), Jinan 250353, China

[b] College of Material Science and Engineering, Shandong University of Science and Technology, Qingdao 266590, China

[c] Energy and Environment Laboratory, School of Engineering, University of East Anglia (UEA), Norwich, NR4 7TJ, United Kingdom.

*Corresponding author. Tel. +86 18353108836, E-mail address: hewen1960@126.com (W. He), https://scholar.google.com/citations?user=pBdTfOUAAAAJ&hl=en.

Abstract

The development of sodium-ion batteries with high power density is highly challenging yet critically important in many applications. Herein, we develop sodium-ion batteries with ultrahigh power density by using N-doped hard/soft double-carbon-coated $Na_3V_2(PO_4)_3$ hybrid-porous microspheres as a cathode. A higher working potential of 3.4 V, superior rate capability (93 mA h g^{-1} at 10 C, 81

mA h g^{-1} at 30 C) as well as stable cycling performance (72.9% capacity retention at 10 C after 1000 cycle) are simultaneously achieved. Very impressively, it can deliver pseudocapacitive behavior and a practical energy density of 317 W h kg^{-1} at a power density of 194 W kg^{-1}, which also remains 73.5 W h kg^{-1} even at an ultrahigh power density of 12600 W kg^{-1}. The superior performances can be ascribed to the hybrid-porous microsphere structure, which provide favorable kinetics for bath electron and Na$^+$, large cathode-electrolyte contact area, as well as robust structural integrity. This design provides a promising pathway for developing low-cost sodium-ion batteries with high energy density as well as high power density.

Keywords: N-doped hard/soft double-carbon-coated; Na$_3$V$_2$(PO4)$_3$; hybrid-porous microspheres; high energy density; ultrahigh power density

1. Introduction

The problem of environmental pollution drives people to develop the clean energy storage device such as lithium-sulfur batteries [1,2] and Li–O$_2$ batteries.[3] However, the availability of lithium leads to a quickly rising price of Li resources. In the recent years, the development of high-energy and high-power density sodium-ion batteries (SIBs) is a great challenge for modern electrochemistry [4,5]. Recently, many spherical structure electrode materials, such as P$_2$Na$_{0.7}$CoO$_2$ microspheres [6], carbon-coated Na$_2$MnPO$_4$F hollow spheres [7], mesoporous germanium phosphide microspheres [8], hierarchical (Ni,Co)Se$_2$/CNT hybrid microspheres [9], and so on, have been investigated for SIBs. Construction of these spherical materials has been demonstrated as an effective way to improve simultaneously the energy and power

2

1   density, tap density, rate capability and cyclic stability of SIBs [10-13]. Among them,

2   mesoporous microsphere structure of $Na_3V_2(PO_4)_3$/carbon (NVP/C) nanocomposites

3   is considered to be one of the most effective ways for high energy/power density SIBs

4   [14,15]. Considerable research efforts have been devoted to the fabrication of NVP/C

5   mesoporous microspheres, in which many synthesis methods, such as the solid state

6   synthesis [16], the sol–gel method [17,18], the aerosol synthesis [19] and spray-drying

7   method [20-23], have been investigated. However, those methods cannot satisfy the

8   requirement for high power density and long cycle life of SIB cathodes.

9   Among the various researched cathodes, NASICON-type NVP not only owns an

10   open three-dimensional (3D) framework structure, but possesses excellent structural

11   stability, high V^{3+}/V^{4+} redox couple potential (about 3.4 V vs. Na^+/Na) and good

12   thermal stability. More importantly, it has a high theoretical capacity of 117 mA h g^{-1}

13   and large theoretical energy density (about 394 W h kg^{-1}) [24-27]. However, NVP has

14   poor electronic conductivity, slower ion transport because of larger radius of Na^+ (1.02

15   Å), more sluggish reaction kinetics and larger volume change upon Na^+/Na insertion/

16   extraction, which usually result in limited rate capability and Na storing reversibility.

17   Therefore, many attempts have been made to enhance the electrochemical properties,

18   including metal doping [28,29], various carbon coating [30-33] and reducing the

19   particles size [34,35]. Among these strategies, N-doped carbon coating [36-39] and

20   double-carbon coating [40-42] have been regarded as the most facile and effective

21   routes to enhance the electrochemical property for NVP. Our works have also

22   demonstrated that hard carbon nanospheres and soft carbon material represent the

3

1 most promising electrodes for SIBs due to its high storage capacity and cycling

2 stability [43-46].

3   The researches show that the solvothermal process played an important role to

4 control the morphology and composition of electrode materials by changing the

5 concentration of catalyst and solvent [47,48]. Herein, N-doped hard/soft

6 double-carbon-coated $Na_3V_2(PO_4)_3$ hybrid-porous microspheres (N-HSDC/NVP-HMs)

7 were prepared by a solvothermal-assisted carbothermal reduction method. This unique

8 microsphere-like structure possesses excellent structural stability, which can bear a

9 huge voltage change during Na^+ extraction/insertion processes. Meanwhile, N-doped

10 carbon network and hybrid-porous can provide electron/ion transport pathways.

11 Several merits of this work are as follows: (1) hybrid-porous N-HSDC (about 5.71

12 wt.%) provides high interface areas for the insertion/extraction of Na ions and high

13 permeability of Na ions and electrolyte; (2) unique microsphere-like structure not

14 only is the most significant factor for improving simultaneously the energy and power

15 density and tap density, but could be used as a stable scaffold for high rate capability

16 and cyclic stability; (3) N-doping (0.83 wt.%) in N-HSDC/NVP-HMs can enhance

17 electric conductivity by adjusting the surface functional groups [36-39]; (4) not only

18 is the solvothermal process simple and cost effective, it is also the most effective

19 method to control the microsphere-like structure. Owing to these merits, as cathode

20 for SIBs, N-HSDC/NVP-HMs shows superior rate performance, remarkable power

21 density and excellent cycling stability (Table S1 in Supporting Information).

22 **2. Experimental Section**

4

1   **2.1 Materials Synthesis**

2   The N-HSDC/NVP-HMs were prepared by a solvothermal-assisted carbothermal

3   reduction method. We used V_2O_5 (99%, Tianjin Kermel Chemical Reagent Co., Ltd),

4    $H_2C_2O_4 \cdot 2H_2O$ (99.5%, Tianjin Bodi Chemical Co., Ltd), H_3PO_4 (99.5%, Shanghai

5   Macklin Biochemical Co., Ltd), CH_3COONa (99.0%, Tianjin Guangfu Technology

6   Development Co., Ltd), ethylene glycol (EG, 99.5%, Tianjin Zhiyuan Chemical

7   Reagent Co., Ltd) and ethylenediamine (EN, AR, Tianjin Damao Chemical Reagent

8   Co., Ltd) as raw materials. The fabrication process by using EN and EG as mixed

9   solution (volume ratio of EG/EN=1:1) is illustrated in Fig. S1 (Supporting

10   Information). Firstly, 0.01 mol of V_2O_5 and 0.03 mol of $C_2H_2O_4 \cdot 2H_2O$ were dissolved

11   into 50 mL deionized water under stirring at 80 °C for 10 min to obtain a homogenous

12   and transparent VOC_2O_4 precursor solution. Then H_3PO_4 (0.03 mol) and CH_3COONa

13   (0.03 mol) were dissolved into the VOC_2O_4 precursor solution with continuously

14   stirred for 30 min to form the NVP precursor solution. Whereafter, EG (5 mL) and EN

15   (5 mL) were dropwise added to the NVP precursor solution, respectively, vigorous

16   stirring for 30 min until a dark green solution was formed. After that, the dark green

17   mixed liquid was transferred into a 100 mL Teflon-lined stainless steel autoclave and

18   kept at 180 °C for 12 h in an electric oven, and then cooled naturally to room

19   temperature. After the solvothermal reaction, a N-HSDC/NVP-HMs precursor

20   solution was collected and dried at 60 °C in air oven. The N-HSDC/NVP-HMs

21   precursor powder after drying was preheated at 350 °C for 5 h in nitrogen atmosphere.

22   After fully grinding, the preheated material was calcined at 800 °C for 8 h in nitrogen

5

1 atmosphere with a heating rate of 5 °C min^{-1} to obtain the black

2 N-HSDC/NVP-HMs-1 (6 mL EG/EN mixed solution), N-HSDC/NVP-HMs-2 (10 mL

3 EG/EN mixed solution) and N-HSDC/NVP-HMs-3 (16 mL EG/EN mixed solution).

4 For comparison, the NVP/C (1 g glucose as carbon source) and pure NVP without any

5 carbon source were also prepared under the same procedure that described above.

6 **2.2 Characterization**

7 The crystalline phase compositions of the as-synthesized samples were identified

8 by X-ray diffraction (XRD) analysis using a Cu-Ka X-ray diffractometer (PANalytical

9 X'Pert PRO; Netherlands). The diffraction patterns were collected over a diffraction

10 angle 2θ range of 10−60° with a scan rate of 5° per min. The morphologies and

11 elemental distributions and composition of the as-synthesized samples were measured

12 by scanning electron microscopy (SEM, JEOL JSM-7100F, 10 Kv) with elemental

13 mapping. The fine microstructure was observed on a transmission electron

14 microscopy (TEM, JEM-2100). The property of carbon was investigated by a Raman

15 microscopic instrument (Renishaw) equipped with an Ar^{+} laser (λ=532 nm) at 50 ×

16 aperture. An automatic surface area analyzer (Micromeritics, Gemini V2380, USA)

17 was used to measure the specific surface area and pore size distribution of the

18 as-synthesized samples. The particle size distributions of the synthesized samples

19 were measured by AS-2011 Laser diffraction particle size analyzer (LDPSA).

20 **2.3 Electrochemical evaluation**

21 The electrochemical performances were characterized with CR 2032-type coin

22 cells assembled in high-purity argon filled glove box where the concentration of both

oxygen and moisture were kept below 1 ppm. In order to prepare cathodes for SIBs, 80% active materials were mixed with 10% poly-vinylidene fluoride (PVDF) and 10% acetylene black in 1 mL N-methyl-2-pyrrolidone (NMP) with continuously stirring overnight. The mixed slurry was coated on aluminum foil with a thickness of about 0.02 mm, dried at 110 °C for 12 h in a vacuum oven and cut into circular strips with diameters of 15 mm. The average load of cathodes is about 1.22 mg cm^{-2}.1 M NaClO$_4$ was dissolved in ethylene carbonate (EC)/propylene carbonate (PC) with a volume ratio of 1:1 as the electrolyte. Glass fibers (Whatman) as the separator and sodium metal as the counter anode. The galvanostatic charging/discharging testings were carried out in the voltage range from 0.5 to 4.5 V at different current densities on channels battery analyzer (CT3008W). The cyclic voltammograms (CV) and electrochemical impedance spectroscopy (EIS) measurements were performed on a CHI-660e electrochemical workstation. All the tests were performed at room temperature.

3. Results and discussion

1.1 Structural characterization and synthesis mechanism

N-doped hard/soft double-carbon-coated Na$_3$V$_2$(PO$_4$)$_3$ hybrid-porous microspheres (N-HSDC/NVP-HMs) were synthesized by a solvothermal-assisted carbothermal reduction method. In the synthesis of N-HSDC/NVP-HMs, ethylenediamine (EN) and ethylene glycol (EG) are used as a multifunctional template of mixed solution, carbon source and structure-directing agent. Solvothermal treatment of the mixture solution at 180 °C for 12 h leads to the formation of microsphere precursor. The morphology

1   and the exact phase structure of NVP precursor after the solvothermal treatment are

2   revealed by SEM images and XRD pattern, respectively. Clearly, the NVP precursor

3   displays a typical spherical morphology with the size range from 4 to 10 μm (Fig.

4   1ab). The enlarged SEM image (Fig. 1c) further reveals the features of the

5   microsphere morphology and hierarchical porous structure of the precursor, which are

6   composed of flakes loosely interconnected with apparent open spaces between them.

7   In the 2θ range of 15–35°, the XRD pattern of NVP precursor after the solvothermal

8   treatment shows a broad bump, indicating the amorphous nature of NVP precursor

9   (Fig. S5A). The strong diffraction peaks in Fig. S5B show that the amorphous NVP

10 precursor spheres were transformed into the NVP crystalline particles by the

11 solvothermal-assisted carbothermal reduction method. The successful formation of

12 the microsphere morphology is due to the self-assembly function of the EG/EN

13 multifunctional template. The solvothermal treatment can create a spherical scaffold

14 geometry with a controlled, porous architecture by adjusting the solvent molecules

15 [47,48].

16   A possible formation mechanism for the precursor microspheres assembled by

17 flakes is showed in Fig. 1d-f. Fig. 1d shows a schematic plot of the functional groups

18 of EN and EG. When EG and EN were dropwise added to the NVP precursor solution,

19 respectively, the EN and EG molecules self-assemble and interconnect with VO^{2+} and

20 PO_4^{3-} ions due to strong electronic/chemical adsorption force of the functional groups,

21 resulting in formation of spherical micelles (Fig. 1e). In the solvothermal reaction

22 process, several concurrent reactions, such as dehydrogenation, condensation,

hydrogen transfer and isomerization, occur at certain temperature and pressure, and

NVP crystal nucleus were formed by heterogeneous nucleation (Fig. 1f). In the heat

treatment process at high temperature, not only are the EN and EG in the spherical

micelles decomposed to form the network structure of hard carbon and soft carbon,

but the residual N and H from the EN and EN were doped into the network structure

in situ, leading to the formation of N-HSDC/NVP-HMs (Fig. 1g). N-HSDC can not

only restrict the growth of NVP nanoparticles and prevent their aggregation, but also

buffer the volume change of NVP particle during sodiation/desodiation process. The

NVP nanoparticles are homogeneously embedded and anchored in the network

structure of N-HSDC (Fig. 1h), which can greatly enhance the electrochemical

performance because of the higher electrical conductivity and fast transfer paths of

electrons and Na^+ ions in the internal structure of microspheres (Fig. 1i) .

The amount of EN/EG template will influence the chemical reaction and

coordination state of the various ionic groups with EG and EN molecules and OH

group, resulting in the formation of N-HSDC/NVP-HMs with different morphology

and structure. The SEM images of the different samples after annealing under

nitrogen at 800 °C for 8 h are shown in Fig. 1j-l. It is found that all the sample

particles were spherical, with different degree of sphericility, different dispersibility,

different porous structure and aggregation behavior. Fig. 3k shows the SEM image of

the N-HSDC/NVP-HMs-2 sample synthesized with 10 mL EG/EN mixed solution. It

is seen that the N-HSDC/NVP-HMs-2 sample can inherit the microsphere

morphology of the precursors and exhibit good degree of sphericility and

1 dispersibility, with a size of 4−8 μm, no obvious agglomeration occurred compared

2 with the N-HSDC/NVP-HMs-1 and N-HSDC/NVP-HMs-3. Some spherical primary

3 particles are uniformly located on the surface of the microsphere (inset of Fig. 3k).

4 However, both the N-HSDC/NVP-HMs-1 and N-HSDC/NVP-HMs-3 have different

5 degrees of agglomeration and larger particle size (Fig. 1jl).

6 The crystal structure, dispersibility and porous structure of the different samples

7 were characterized by X-ray diffraction (XRD), N_2 adsorption/desorption isotherm

8 and laser particle size analyzer, respectively, as shown in Fig. 2a-f. XRD patterns of

9 all the samples are displayed in Fig. 2a. The diffraction peaks of all the samples can

10 be readily indexed to the rhombohedral $Na_3V_2(PO_4)_3$ phase (JCPDS No. 62-0345,

11 space group R3c) without impurities, indicating that pure-phased crystal were

12 synthesized [28,29]. The unit cell parameters of the different samples are given in

13 Table S2. From the calculated results, the cell volume of spherical

14 N-HSDC/NVP-HMs samples are more smaller than those of unspherical NVP/C and

15 NVP samples, which indicated that solvothermal makes cell volume decline slightly.

16 Especially, N-HSDC/NVP-HMs-2 has the smallest cell volume compared with the

17 other samples, indicating a more stable structure approached to the standard

18 NASICON phase, which contributes to its cycling properties [31]. Moreover, the

19 comparison of unit cell parameters of N-HSDC/NVP-HMs-2 and various

20 $Na_3V_2(PO_4)_3$ (NVP) samples reported in the literatures is recorded in Table S3. The

21 result shows that the cell volume of N-HSDC/NVP-HMs-2 is much smaller than those

22 reported in the literatures, showing that the spherical NVP particles in

10

1   N-HSDC/NVP-HMs-2 have more stable structure. The particle size distributions of

2   the different samples were measured by LDPSA, as shown in Fig. 2b-d and

3   summarized in Table S4. The N-HSDC/NVP-HMs-2 sample has a smaller particle

4   size distribution, and the particle size has a log-normal distribution with an average

5   diameter of 4.71 μm (Fig. 2c) compared with the N-HSDC/NVP-HMs-3. However,

6   the N-HSDC/NVP-HMs-3 has two particle size distributions (3−8μm and 12−96 μm),

7   indicating that there exist obvious aggregation (Fig. 2d). Fig. 2e shows that the

8   nitrogen adsorption-desorption sorption isotherms of different samples. All the

9   samples show the same isotherms (type-IV) and H3-type hysteresis loop caused by

10   non-uniform wormlike pores, implying the typical mesopore characteristics [43,44].

11   The pore-size-distributions of these samples were further investigate by

12   Barret-Joyner-Halenda (BJH) model, all showing the two pore size distributions of

13   1.75−2 nm (micropore structure) and 2−4.5 nm (mesoporous structure) (Fig. 2f). This

14   hybrid-porous structure of the N-HSDC/NVP-HMs-2 was also observed with

15   HRTEM (Fig. 3b). These micropores can provide strain space to buffer the volume

16   expansion/contraction of NVP, sequentially leading to a good cycling stability. These

17   mesopores are mainly contributed from the interstices among the assembled

18   nanoparticles, not only can be well permeated by electrolyte, but also can act as

19   efficient transfer channels of Na^+ [43]. Brunauer-Emmett-Teller (BET) surface area of

20   different samples is measured and summarized in Table S5. The

21   N-HSDC/NVP-HMs-2 has the highest specific surface areas of 40.5 $m^2\,g^{-1}$ owing to

22   good degree of sphericility and dispersibility (Fig. 1j). The lower EG/EN added

11

1 volume result in poor uniformity (Fig. 1k), so that the specific surface area of

2 N-HSDC/NVP-HMs-1 is undesirable (13.5 $m^2\ g^{-1}$). However, severe agglomeration

3 was occurred because of adding EG and EN overmuch (shown in Fig. 1l and Fig. 2d),

4 so that the specific surface area of N-HSDC/NVP-HMs-3 became lower compared

5 with N-HSDC/NVP-HMs-2. It is well known that high specific surface area of

6 cathode material can increase the contact area between the cathode and the electrolyte,

7 which is beneficial to improve its rate performance [43,44]. Therefore, the

8 N-HSDC/NVP-HMs-2 cathode possesses the best rate performance than other

9 samples at higher rates of 20-50 C (Fig. 5d).

10 The element content in the different samples was determined by a Vario EL

11 IIICHN elemental analyzer and summarized in Table S6. The results show that the

12 element contents of C, N and H elements all increase with the additive amount of

13 EG/EN mixed solution, which indicates that C, N and H elements both come from EG

14 and EN. Among them, C element is the main component of double-carbon structure,

15 while most of H element exists at the border of the double-carbon structure to saturate

16 the carbon bond, which is favorable to increase the concentration of itinerant electrons

17 and improve electrochemical activity of carbon structure [49]. The structure of N

18 element in N-HSDC/NVP-HMs-2 sample was further investigated by using XPS N1s

19 spectrum (shown in Fig. 2j). The carbon content in N-HSDC/NVP-HMs-2 sample is

20 4.88 wt%. The deficiency and over capacity of carbon content in the

21 N-HSDC/NVP-HMs samples all affect the high rate performance and long circle life

22 of cathodes (Fig. 5). Raman spectrum was also carried out to further investigate the

12

1   nature of the carbon-network in N-HSDC/NVP-HMs-2 (Fig. 2g). Two broad peaks

2   which were found at the ranges of 1200–1800 cm^{-1} can be deconvoluted by three

3   Gaussian peaks. The Gaussian peaks located at around 1300 and 1600 cm^{-1} are

4   assigned to the D (disordered carbon) and G (graphitized carbon) bands of carbon,

5   respectively. The value of the peak intensity ratio of D to G band (I_D/I_G) is 1.57,

6   indicating that the disordered hard carbon has a higher fraction (about 55.05% area) in

7   the residual carbon [50]. The third Gaussian peak around 1530 cm^{-1} is attributed to

8   soft carbon according to the previous reports [51], which has a fraction of about 33.67%

9   (area) in the residual carbon. In addition, some weak bands located around 1000 cm^{-1}

10   belong to the stretching vibrations of PO_4^{3-}.

11   The X-ray photoelectron spectroscopy (XPS) was carried out to characterize the

12   elemental components and chemical state of N-HSDC/NVP-HMs-2. As shown in Fig.

13   2h, P, C, N, V, O and Na are discovered in the survey spectrum, which is consistent

14   with the elemental constitute of N-HSDC/NVP-HMs-2. Fig. S2 shows the

15   deconvolution results of XPS V2p spectrum by using two Gaussian curves fitting. The

16   peaks located at 523.8 and 517 eV are assigned to V^{3+} 2p$_{1/2}$ and V^{3+} 2p$_{3/2}$ in the

17   N-HSDC/NVP-HMs-2, respectively [51]. The high resolution XPS C1s spectrum (Fig.

18   2i) of N-HSDC/NVP-HMs-2 can be resolved into four peaks at 284.6, 285.8, 286.9

19   and 289.6 eV (Table S7), which are assigned to C-C, C-N, C-O and O-C=O

20   configurations, respectively [28]. The nitrogen doped carbon was further evidenced

21   by the XPS N1s spectrum of N-HSDC/NVP-HMs-2 (Fig. 2j). The XPS N1s spectrum

22   can be divided into three peaks at 398.6, 401.1 and 403.4 eV (Table S8),

13

1 corresponding to pyridinic nitrogen (N1), pyrrolic nitrogen (N2) and graphitic

2 nitrogen (N3), respectively [52]. On the one hand, N1 and N2 were formed by

3 replacing C atom with N atom in hexagonal and pentagonal rings, respectively.

4 Meanwhile, these two kinds of replacements could result little damage to carbon

5 skeletons and bring some "holes" structures or amorphous carbon. N2 contributes one

6 pair of lone electrons to the matrix carbon which can improve the electronic

7 conductivity of amorphous carbon. On the other hand, the formation of N3 via

8 substituting C atom by N atom accompany without destruction to carbon skeletons

9 [55]. In order to clearly describe the mechanism of N-doped carbon, the model of the

10 N-modificatory carbon matrix is exhibited in the inset of Fig. 2j. Besides, the peak

11 relative intensity of N1 and N2 are much higher than that of N3, indicating that large

12 amount of N1 and N2 are embedded into N-HSDC network. According to the XPS

13 data, the atomic percentage of N1, N2 and N3 are 44.01 at%, 46.48 at% and 9.51 at%,

14 respectively.

15   The microstructure of N-HSDC/NVP-HMs-2 sample is characterized by HRTEM.

16 The TEM images of N-HSDC/NVP-HMs-2 sample show that its hierarchical

17 hybrid-porous microsphere structure is composed of the spherical primary particles

18 to adhere to each other and (Fig. 3ab). The spherical primary particles have an

19 average diameter of about 100 nm (Fig. 3b). The enlarged TEM image (Fig. 3c)

20 further reveals the detailed features of a primary particle in the microsphere structure.

21 Fig. 3c clearly shows the lattice fringes with the space of 6.2 Å, corresponding to the

22 (102) crystal plane of NVP, also demonstrates that the soft carbon and spherical hard

1 carbon nanoparticles (about 5–25 nm) are well decorated on the surface of NVP

2 crystal. Fig. 3c also displays the disordered structure of hard carbon and vermicular

3 texture of soft carbon on certain orientation. The scanning electron microscopy (SEM)

4 and X-ray energy dispersive spectrometry (EDS) analyses were used to further

5 characterize the components in the microspheres. The elemental mapping images of

6 the N-HSDC/NVP-HMs-2 sample confirm further the existence and uniform

7 distribution of N, Na, O, P, V and C in a microsphere, the carbon-coating and

8 nitrogen-doping (Fig. 3d-j).

9   The effect of the carbon's microstructure on the Na^+ diffusion and

10 electrochemical performances is schematically described in Fig. 4. According to the

11 previous report, the ordered carbon clusters with enlarged interlayer distance play a

12 critical role to the rapid Na^+ solid diffusion in carbon structure.[53] The soft carbon

13 with ordered N-doped carbon clusters are favorable to reducing the ion diffusion

14 resistance (Fig. 4a). Besides, hard carbon with randomly oriented graphitic layers and

15 short-range ordered structure in plane can act as the superior conductive intermediary

16 for charge transmission (Fig. 4b) [54]. As expected, the N-HSDC/NVP-HMs has the

17 lower ion diffusion resistance (Table S9) and superior Na^+-storage performances (Fig.

18 6) compared with NVP/C sample because of the coexistence of hard carbon and soft

19 carbon (Fig. 4c).

20 **3.2 Electrochemical measurements**

21 In order to optimized preparation conditions, the electrochemical performances of the

22 different cathodes were investigated by assembling half-cells using sodium metal as

15

1   Galvanostatic charge-discharge tests, CV and EIS techniques are employed to

2   evaluate the electrochemical reaction kinetics of all cathodes. The electrochemical

3   property comparison of different cathodes synthesized with different amount of

4   EG/EN mixed solution is shown in Fig. 5. Fig. 5a show the first charging/discharging

5   profiles of different cathodes at a current rate of 10 C (1 C refers to a current density

6   of 117 mA g^{-1}) over a voltage range of 2.0–4.0 V. All cathodes exhibits a

7   charging/discharging plateau at around 3.4 V, which is consistent with the that of NVP

8   cathode reported previously [28,29]. A reversible capacity of 92.9 mA h g^{-1} for

9   N-HSDC/NVP-HMs-2 can be acquired under a current rate of 10 C, corresponding to

10   about 91.3% of the initial capacity at 0.5 C. The CV curves of different cathodes at a

11   scanning rate of 0.1 mV s^{-1} in the potential region of 2.0–4.0 V are shown in Fig. 5b.

12   All cathodes have an oxidation peak located at ≈3.50 V and a distinct reduction peak

13   at ≈3.28 V, which can be assigned to the de-intercalation/intercalation of Na^+ caused

14   by the reversible transformation of V^{4+}/V^{3+} redox reaction. However, the split peaks

15   located at ≈3.12 V and ≈3.28 V for N-HSDC/NVP-HMs-1 and N-HSDC/NVP-HMs-3

16   are probably associated with a local redox environment rearrangement from the

17   transfer of Na(1) to Na(2), which has been found in other NASICON materials

18   structured frameworks, such as $Na_3M_2(PO_4)_3$ (M: Sc, Cr, Fe) [55,58].

19   The Nyquist plots of the different cathodes before cycling for the frequencies

20   ranging from 10 Hz to 100 kHz during the discharge state are displayed in Fig. 5c. A

21   semicircle in the high frequency region and a straight line in the low frequency region

22   were found in each of the Nyquist plots for all cathodes. The EIS results imply that

16

1 the electrochemical process is controlled by both charge transfer impedance (R_{ct}) on

2 the cathode/electrolyte interface and sodium-ion diffusion impedance (Z_w) in the bulk

3 of the cathode materials. It is obvious that the N-HSDC/NVP-HMs-2 cathode exhibits

4 much lower R_{ct} (R_{ct}=122 Ω) than that of N-HSDC/NVP-HMs-1 (421 Ω) and

5 N-HSDC/NVP-HMs-3 (314 Ω) cathodes, indicating that the proper content of

6 N-doped carbon is beneficial for the efficient transport of electrons and leads to lower

7 resistance. And the Na$^+$ diffusion coefficient (D_{Na+}) could be calculated as:

8 $$D_{Na+} = \frac{R^2 T^2}{2A^2 n^4 F^4 C^2 \sigma^2}$$ (1)

9 $$Z' = R_s + R_{ct} + \sigma\omega^{-1/2}$$ (2)

10 where R is the gas constant, T is the absolute temperature, F is Faraday constant, A is

11 attributed to area of electrode surface, C is concentration of Na$^+$, n is the number of

12 electrons. The inset in Fig. 5c shows the linear fitting of Z_{real} $vs.$ $\omega^{-1/2}$ at low frequency

13 region for the three samples. And the Warburg impedance coefficient (σ) can be

14 obtained by calculating the relationship between real impedance (Z') and the

15 reciprocal square-root of frequency ($\omega^{-1/2}$), from the eq (2). Furthermore, the R_{ct} and

16 D_{Na+} of different cathodes are listed in Table S9. As was revealed, the

17 N-HSDC/NVP-HMs-2 cathode behaves the highest D_{Na+} (2.67×10^{-12} cm^2 s^{-1}),

18 indicating that the N-HSDC can effectively improve electrochemical kinetics. Fig. 5d

19 and Fig. S3a-c compare the rate property of the different cathodes at various current

20 rates. The results show that the N-HSDC/NVP-HMs-1 cathode shows the higher

21 initial specific discharge capacity (Fig. S3a) in the lower rate range of 0.1–10 C.

22 However, the N-HSDC/NVP-HMs-2 cathode displays much higher reversible

17

capacity than the N-HSDC/NVP-HMs-1 and N-HSDC/NVP-HMs-3 cathodes at the

high rate range of 20–50 C (Fig. 5d).

In order to evaluate the potential for practical applications, we calculated the

power and energy densities of the different cathodes from the discharge curves based

on the capacities at various rates, working potential and the mass of cathode material.

The power density (P, W kg^{-1}) of cathodes is calculated by the following formulae

[57]:

$$P = \frac{E \times 3600}{\Delta t} \tag{3}$$

E is specific energy (W h kg^{-1}) and Δt is the time of discharge (s). By comparing the

rate property and energy density of different cathodes at various C-rate, it can be seen

that the N-HSDC/NVP-HMs-2 cathode not only has high rate property at the high

C-rate range of 20–50 C (Fig. 5d), but it also delivers surpassing energy density (Fig.

5e). Fig. 5f shows the Ragone plot (energy density vs. power density) of different

cathodes in the voltage range of 2.0–4.0 V. The results show that the energy density

and power density of N-HSDC/NVP-HMs-2 cathode are superior to other cathodes.

The N-HSDC/NVP-HMs-2 cathode has a high energy density of 317 W h kg^{-1} at a

power density of 194 W kg^{-1} (0.5 C), which also remains 73.5 W h kg^{-1} even at an

ultrahigh power density of 12600 W kg^{-1} (Table S10). Furthermore, Fig. 5g shows the

long-life performance comparison of different cathodes at a current density of 10 C.

The N-HSDC/NVP-HMs-1, N-HSDC/NVP-HMs-2 and N-HSDC/NVP-HMs-3

cathodes display the discharge capacities of 100.8, 92.9 and 85.3 mA h g^{-1} at first

cycle, respectively. However, the N-HSDC/NVP-HMs-2 cathode shows the highest

1 capacity retention (72.9 %) over 1000 cycles, but the corresponding capacity

2 retentions of N-HSDC/NVP-HMs-1 and N-HSDC/NVP-HMs-3 are only 28.2 % and

3 29.0% over 1000 cycles, respectively.

4   In order to verify the advantage of the unique microsphere-like structure of the

5 N-HSDC/NVP-HMs-2 cathode, the Na$^+$-storage performances of the

6 N-HSDC/NVP-HMs-2 cathode were investigated by the electrochemical property

7 comparison of different cathodes with different structure. Fig. 6a shows the initial

8 discharge-charge curves of different cathodes at 0.5 C in the voltage range from 2.0 to

9 4.0 V. The N-HSDC/NVP-HMs-2 cathode shows a flat voltage plateau with smaller

10 polarization around 3.3 V and the higher initial specific discharge capacity (101.8 mA

11 h g^{-1}), which is characteristic of the two-phase Na insertion/extraction reactions.

12 However, both the NVP/C and bare NVP cathodes displayed sloping discharge/charge

13 profiles with larger potential range and the lower discharge capacity at the same rate.

14 Fig. 6b and Fig. 6c compare the rate property and the energy density of the different

15 cathodes at various current rates, respectively. The N-HSDC/NVP-HMs-2 cathode

16 displays much higher reversible capacity and energy density than the NVP/C and bare

17 NVP cathodes at the same rates. Especially when the current rates

18 increase continuously from 0.5 C to 30 C, the attenuation rate of its discharging

19 capacity and energy density is very low. Fig. 6d shows the initial discharge-charge

20 curves of N-HSDC/NVP-HMs-2 cathode were also investigated at the different

21 current rates in a relatively wide voltage range of 0.5–4.5 V. The discharging capacity

22 of N-HSDC/NVP-HMs-2 can reach 180 mA h g^{-1} at 0.1 C, which is much higher than

1   the theoretical capacity of NVP (117 mA h g^{-1}).

2   Fig. 6e displays that the CV curve of N-HSDC/NVP-HMs-2 cathode has a

3   couple of more symmetrical redox peaks than the NVP/C and bare NVP cathodes at

4   the same scanning rate and the potential region, This shows that the

5   N-HSDC/NVP-HMs-2 cathode exhibits high kinetic behavior owing to its high

6   conductive network of N-HSDC in the microsphere structure. To better understand the

7   improved performance by N-HSDC, EIS of the different cathodes were carried out

8   after the first discharge (Fig. 6f). Obviously, the N-HSDC/NVP-HMs-2 cathode

9   exhibits much lower R_{ct} (122 Ω) than that of NVP/C (433 Ω) and NVP (921 Ω). The

10   results obtained from inset in Fig. 6f show that the D_{Na+} value (2.67×10^{-12} cm^2 s^{-1}) of

11   the N-HSDC/NVP-HMs-2 cathode is much high than that of NVP/C (5.83×10^{-15} cm^2

12   s^{-1}) and NVP (1.71×10^{-14} cm^2 s^{-1}), indicating that the electrochemical kinetics of

13   N-HSDC/NVP-HMs-2 is easier with Na$^+$ extraction than NVP/C and NVP. These

14   results further prove the advantage of the unique microsphere-like structure of the

15   N-HSDC/NVP-HMs-2 cathode. Additionally, the N-HSDC/NVP-HMs-2 cathode also

16   exhibits exceptionally high coulombic efficiency, which is close to 100%, indicating

17   its superior phase reversibility during repeated extraction/insertion of Na$^+$ even at

18   long-term high-rate cycling (8898 cycles at 10 C). This structural stability is further

19   confirmed by the XRD pattern of N-HSDC/NVP-HMs-2 after undergoing 8898 cycles,

20   as seen in Fig. S5C. In the XRD pattern the major diffraction peaks of NVP are almost

21   visible, demonstrating this electrode material may reversibly cycle in a relatively wide

22   potential window of 0.5–4.5 V. However, it has lower cyclability at long-term

20

1 high-rate cycling, showing only a discharge capacity retention of 8.53% % after 8898

2 cycles at 10 C (Fig. 6g). Furthermore, the N-HSDC/NVP-HMs-2 cathode displays the

3 initial discharge capacity of 91.5 mA h g^{-1} at 20 C and keeps a capacity retention of

4 46.4% after 600 cycles (Fig. 6h). The excellent high rate capability of

5 N-HSDC/NVP-HMs-2 cathode can be ascribed to the advantages of its unique

6 microsphere-like structure as a stable scaffold, hybrid-porous structure as efficient

7 transfer channels of Na^+, N-HSDC with high conductivity and interface areas and

8 high active NVP nanoparticles with the large electrode–electrolyte contact area and

9 short ion diffusion distance.

10   Fig. S3a-e deliver the charge-discharge curves of different cathodes in the

11 voltage range of 2.0–4.0 V at various current rates from 0.1 C to 10 C. The curves of

12 N-HSDC/NVP-HMs-2 cathode show a low dropping of discharge capacity and small

13 polarization. The CV curves of different cathodes at different scanning rates in the

14 potential region of 2.0-4.0 V are shown in Fig. S4a-c. As the scan rate increase, the

15 double reduction peaks of all cathodes disappear gradually and anodic potential shifts

16 to higher voltages and cathodic potential shifts to lower voltages. We supposed this

17 phenomenon can be attributed to the active Na^+ ion sites cannot be clearly identified

18 any more with high scan speed and the increased polarization at higher scan rates due

19 to kinetic limitations associated with Na^+ diffusion through the active material. The

20 N-HSDC/NVP-HMs-2 cathode shows a battery-like behavior, so its total charge came

21 mainly from the diffusion-controlled process in the potential region of 2.0-4.0 V.

22   To get further insights into the influence of the hybrid-porous microsphere

structure and N-HSDC on the electrochemical performances, the CV curves of different cathodes were also measured at different scanning rates from 0.1 to 1.0 mV s^{-1} in a lower voltage range (0.01–1.2 V) (Fig. S4d-f). All CV curves exhibit a nearly rectangular morphology without distinct redox peaks, showing similar electrochemical behavior of electric double layer (EDL) capacitors. This is characteristic of a surface-confined charge transfer process [57]. Hence, they also possess intercalation pseudocapacitive of surface-controlled processes due to the emergence of extrinsic faradaic reactions in the carbon structure [57].

Pseudocapacitive behavior enables ultrafast charge/discharge kinetics and substantially higher energy storage. [58]. In order to understand well the excellent rate capability and power density of N-HSDC/NVP-HMs-2 cathode, the CV curves in a wide voltage range (0.5–4.5 V) are also be used to identify the pseudocapacitive behavior by changing scanning rate from 0.2 to 0.5 mV s^{-1} (Fig. 7a). The capacitive contributions of total stored charge can be described by (4):

$$i = av^b \tag{4}$$

where i and v are the measured current and versus sweep rate from CV data. a and b are the adjustable parameters, where b is quite pivotal. $b = 0.5$ reflects a diffusion-controlled process, while $b = 1.0$ implies a surface-controlled process. Generally, b value locates between 0.5 and 1.0, suggesting a mixed contribution of both processes. The value of b can be obtained by the slope of the plot of log i vs. log v according to the equation (5).

$$\log i = b \log v + \log a \tag{5}$$

1   In our case, *b* values of the cathodic and anodic peaks are 0.69 and 0.73 (Fig. 7b),

2   indicating that a part of capacity contribution was from a surface-controlled process.

3   The capacity contribution from capacitive and diffusion-controlled charge could be

4   defined on the basis of the relationship：

5    $i = k_1 v + k_2 v^{1/2}$ (6)

6   where $k_1 v$ is the contribution from surface capacitances and $k_2 v^{1/2}$ is the contribution

7   from diffusion-controlled processes. Using the equation (6), we can identify the ratio

8   of the two processes in the entire potential window. As shown in Fig. 7c, with the

9   increase from 0.2 to 0.5 mV s^{-1} in the sweep rates, the contribution of capacitive

10   charge rises from 6 % to 13.8%. The results show that N-HSDC/NVP-HMs-2 cathode

11   displays battery-like and pseudocapacitive behaviour by the refined control of the

12   working potential due to its unique hybrid-porous microsphere structure.

13   With the above consideration, we can expatiate the reaction mechanism for the

14   "pseudocapacitive behaviour" of Na$^+$ storage in N-HSDC/NVP-HM (Fig. 8). This

15   reaction mechanism contains intrinsic battery behavior of NVP microsphere and

16   extrinsic pseudocapacitive behavior of N-HSDC. N-HSDC provides extra Na ion

17   intercalation via adsorption and electrostatic accumulation of charges (Fig. 8a).

18   During the charge/discharge processes, bulk redox reactions occur at the battery-type

19   NVP microsphere, showing high energy density. The arrangement of the charges in

20   N-HSDC results in a displacement current and faradaic reactions with fast charge

21   transfer, increasing the power density because of the short ion and electron transport

22   paths [57], at the meantime, the electrons flow across the external circuit (Fig. 8b).

23

Therefore, different charge storage mechanisms of N-HSDC/NVP-HMs cathodes contribute to the excellent rate capability, high power density and long life span, revealing its wide application in SIBs with high power [59,60]. This is of particular interest for designing high-power energy storage devices based on traditional high-energy density NVP via controlling different surface intercalation reactions and morphology.

4. Conclusion

In summary, low-cost N-doped hard/soft double-carbon-coated $Na_3V_2(PO_4)_3$ hybrid-porous microspheres (N-HSDC/NVP-HMs) were prepared by a solvothermal-assisted carbothermal reduction method. We studied the Na^+ storage property of N-HSDC/NVP-HMs, which can function as superfast cathode materials for high-energy and high-power density sodium-ion batteries (SIBs). Moreover, a pseudocapacitive behavior of N-HSDC/NVP-HMs was produced by the refined control of the working potential. Remarkably, the N-HSDC/NVP-HMs not only deliver higher working potential, superior rate capability as well as stable cycling performance, but also exhibit an exceptional combination of energy and power densities among existing batteries and capacitors, offering an ultrahigh power density of 12600 W kg^{-1} while maintaining an energy density of 73.5 W h kg^{-1}. These excellent electrochemical performances could be attributed to the synergistically enhance of microsphere structure and N-doped hard/soft double-carbon-coated layer. This work not only presents a highly promising energy storage paradigm for low-cost and scalable higher-power application of SIBs, but also could be extended to the

24

1   design of other cathode materials.

2

References

4   [1] R.W. Yi, C.G. Liu, Y.C. Zhao, L.J. Hardwick, A light-weight free-standing

5   graphene foam-based interlayer towards improved Li-S cells, Electrochim Acta

6   299 (2019) 479–488.

7   [2] R.W. Yi, X.F Lin, Y.C. Zhao, C.G. Liu, Y.Q. Li, L.J. Hardwick Fabrication of a

8   Light-Weight Dual-Function Modified Separator towards High-Performance

9   Lithium-Sulfur Batteries, ChemElectroChem 6 (2019) 3648–3656.

10   [3] P.G. Bruce, S.A. Freunberger, L.J. Hardwick, J.M. Tarascon, Li–O_2 and Li–S

11   batteries with high energy storage, Nat. Mater. 11 (2012) 19–29.

12   [4] S. Wu, C. Liu, D.A. Dinh, K.S. Hui, K.N, Hui, J.M, Yun, K.H, Kim,

13   Three-Dimensional Self-Standing and Conductive $MnCO_3$@Graphene/CNT

14   Networks for Flexible, Asymmetric Supercapacitors, ACS Sustainable Chem.

15   Eng. 711 (2019) 9763–9770.

16   [5] S. Wu, H. Guo, K.S. Hui, K.N. Hui, Rational design of integrated

17   CuO@$Co_xNi_{1-x}(OH)_2$ nanowire arrays on copper foam for high-rate and

18   long-life supercapacitors, Electrochim. Acta 295 (2019) 759–768.

19   [6] Y. Fang, X.Y. Yu, X.W. Lou, A Practical High☐Energy Cathode for Sodium☐Ion

20   Batteries Based on Uniform P2-$Na_{0.7}CoO_2$ Microspheres, Angew. Chem. Int. Ed.

21   56 (2017) 5801–5805.

22   [7] L. Wu, Y. Hu, X.P. Zhang, J.Q. Liu, X. Zhu, S.K. Zhong, Synthesis of

carbon-coated Na_2MnPO_4F hollow spheres as a potential cathode material for Na-ion batteries, J. Power Sources 374 (2018) 40–47.

[8] K.W. Tseng, S.B. Huang, W.C. Chang, H.Y. Tuan, Synthesis of Mesoporous Germanium Phosphide Microspheres for High-Performance Lithium-Ion and Sodium-Ion Battery Anodes, Chem. Mater. 3013 (2018) 4440–4447.

[9] S. H. Oh, J. S. Cho, Hierarchical $(Ni,Co)Se_2$/CNT hybrid microspheres consisting of a porous yolk and embossed hollow thin shell for high-performance anodes in sodium-ion batteries, J. Alloy. Compd. 806 (2019) 1029–1038.

[10] D.F. Qiu, X. Ma, J.D. Zhang, Z.X. Lin, B. Zhao, Mesoporous Silicon Microspheres Produced from In Situ Magnesiothermic Reduction of Silicon Oxide for High-Performance Anode Material in Sodium-Ion Batteries, Nanoscale Res Lett 13 (2018) 275.

[11] T. Liu, L.Y. Zhang, B. Cheng, J.G. Yu, Hollow Carbon Spheres and Their Hybrid Nanomaterials in Electrochemical Energy Storage, Adv. Energy Mater. 9 (2019) 1803900.

[12] Y.Y. Lu, Q. Zhao, N. Zhang, K.X. Lei, F.J. Li, J. Chen, Facile Spraying Synthesis and High☐Performance Sodium Storage of Mesoporous MoS_2/C Microspheres, Adv. Funct. Mater. 26 (2016) 911–918.

[13] D.F Xu, C.J. Chen, J. Xie, B. Zhang, L. Miao, J. Cai, Y.H. Huang, L. Zhang, A Hierarchical N/S☐Codoped Carbon Anode Fabricated Facilely from Cellulose/Polyaniline Microspheres for High-Performance Sodium☐Ion Batteries, Adv. Energy Mater. 6 (2016) 1501929.

[14] X.X Cao, A.Q Pan, B. Yin, G.Z. Fang, Y.P Wang, X.Z. Kong, T. Zhu, J. Zhou, G.Z. Cao, S.Q. Liang, Nanoflake-constructed porous $Na_3V_2(PO_4)_3$/C hierarchical microspheres as a bicontinuous cathode for sodium-ion batteries applications, Nano Energy 60 (2019) 312–323.

[15] H.Z. Chen, B. Zhang, X. Wang, P.Y. Dong, H. Tong, J.C. Zheng, W.J. Yu, J.F. Zhang, CNT-Decorated $Na_3V_2(PO_4)_3$ Microspheres as a High-Rate and CycleStable Cathode Material for Sodium Ion Batteries, ACS Appl. Mater. Interfaces 10 (2018) 3590–3595.

[16] Z.L. Jian, L. Zhao, H.L. Pan, Y.S. Hu, H. Li, W. Chen, L.Q. Chen, Carbon coated $Na_3V_2(PO_4)_3$ as novel electrode material for sodium ion batteries Electrochem. Commun. 14 (2012), 86–89.

[17] S.Y. Lim, H. Kim, R.A. Shakoor, Y. Jung, J.W. Choi, Electrochemical and Thermal Properties of NASICON Structured $Na_3V_2(PO_4)_3$ as a Sodium Rechargeable Battery Cathode: A Combined Experimental and Theoretical Study, J. Electrochem. Soc. 159 (2012) 1393–1397.

[18] Q.Y. Wang, B.D. Zhaoa, S. Zhang, X.H. Gao, C. Deng, Superior Sodium Intercalation of Honeycomb-structured Hierarchical Porous $Na_3V_2(PO_4)_3$/C Microball Prepared by a Facile One-pot Synthesis, J. Mater. Chem. A 3 (2015) 7732–7740.

[19] J.F. Mao, C. Luo, T. Gao, X.L. Fan, Ch.S. Wang, Scalable synthesis of $Na_3V_2(PO_4)_3$/C porous hollow spheres as a cathode for Na-ion batteries, J. Mater. Chem. A 3 (2015) 10378–10385.

[20] J.X. Zhang, Y.J. Fang, L.F. Xiao, J.F. Qian, Y.L. Cao, X.P. Ai, H.X. Yang, Graphene-Scaffolded $Na_3V_2(PO_4)_3$ Microsphere Cathode with High Rate Capability and Cycling Stability for Sodium Ion Batteries, ACS Appl. Mater. Interfaces 9 (2017) 7177–7184.

[21] H.Z. Chen, Y.D. Huang, G.Q. Mao, H. Tong, W.J. Yu, J.C. Zheng, Z.Y. Ding, Reduced Graphene Oxide Decorated $Na_3V_2(PO_4)_3$ Microspheres as Cathode Material With Advanced Sodium Storage Performance, Front. Chem. 6 (2018) 174.

[22] W. Zheng, X.B. Huang Y.R. Rend, H.Y. Wang, S.B. Zhou, Y.D. Chen, X. Ding, T. Zhou, Porous spherical $Na_3V_2(PO_4)_3$/C composites synthesized via a spray drying-assisted process with high-rate performance as cathode materials forsodium-ion batteries, Solid State Ionics 308 (2017) 161–166.

[23] G.Q. Du, S.J. Wang, M. Zheng, 3D CNT decorated $Na_3V_2(PO_4)_3$/C microsphere with outstanding sodium storage performance for Na-ion batteries, Solid State Ionics 317 (2018) 229–233.

[24] Z. Jian, W. Han, X. Lu, H. Yang, Y.S. Hu, J. Zhou, Z. Zhou, J. Li, W. Chen, D. Chen, L.Q. Chen, Superior electrochemical performance and storage mechanism of $Na_3V_2(PO_4)_3$ cathode for room-temperature sodium-ion batteries, Adv. Energy Mater. 3 (2013) 156–160.

[25] S. Li, Y.F. Dong, L. Xu, X. Xu, L. He, L.Q. Mai, Effect of carbon matrix dimensions on the electrochemical properties of $Na_3V_2(PO_4)_3$ nanograins for high-performance symmetric sodium-ion batteries, Adv. Mater. 26 (2014) 3545–

28

3553.

[26] M. Cabello, R. Alcantara, F. Nacimiento, P. Lavela, M. Aragon, J. Tirado, $Na_3V_2(PO_4)_3$ as electrode material for rechargeable magnesium batteries: a case of sodium-magnesium hybrid battery, Electrochim. Acta 246 (2017) 908–913.

[27] J.F. Mao, C. Luo, T. Gao, X.L. Fan, C.S. Wang, Scalable synthesis of $Na_3V_2(PO_4)_3$/C porous hollow spheres as a cathode for Na-ion batteries, J. Mater. Chem. A 3 (2015) 10378–10385.

[28] Q. Zheng, H.M. Yi, W.Q. Liu, X.F. Li, H.M. Zhang, Improving the electrochemical performance of $Na_3V_2(PO_4)_3$ cathode in sodium ion batteries through Ce/V substitution based on rational design and synthesis optimization, Electrochim. Acta 238 (2017) 288–297.

[29] H. Li, X.Q. Yu, Y. Bai, F. Wu, C. Wu, L.Y. Liu, X.Q. Yang, Effects of Mg doping on the remarkably enhanced electrochemical performance of $Na_3V_2(PO_4)_3$ cathode materials for sodium ion batteries, J. Mater. Chem. A 3 (2015) 9578–9586.

[30] S.J. Li, P. Ge, C.Y. Zhang, W. Sun, The electrochemical exploration of double carbon-wrapped $Na_3V_2(PO_4)_3$: Towards long-time cycling and superior rate sodium-ion battery cathode, J. Power Sources 366 (2017) 249–258.

[31] H. Li, Y. Bai, F. Wu, Y. Li, C. Wu, Budding willow branches shaped $Na_3V_2(PO_4)_3$/C nanofibers synthesized via an electrospinning technique and used as cathode material for sodium ion batteries, J. Power Sources 273 (2015) 784–792.

[32] W. Shen, H. Li, Z.Y. Guo, C. Wang, Z.H. Li, Q.J. Xu, H.M. Liu, Y.G. Wang, Y.Y. Xia, Double-nanocarbon synergistically modified $Na_3V_2(PO_4)_3$: an advanced cathode for high-rate and long-life sodium-ion batteries, ACS Appl. Mater. Interfaces 8 (2016) 15341–15351.

[33] X.Q. Chang, Q.Z. Zhu, N. Sun, Y.B. Guan, R. Wang, J.S. Zhao, M.Y. Feng, B. Xu, Graphene-bound $Na_3V_2(PO_4)_3$ film electrode with excellent cycle and rate performance for Na-ion batteries, Electrochim. Acta 269 (2018) 282–290.

[34] H. Li, Y. Bai, F. Wu, Q. Ni, C. Wu, $Na_3V_2(PO_4)_3$/C nanorods as advanced cathode material for sodium ion batteries, Solid State Ionics 278 (2015) 281–286.

[35] H. Li, Y. Bai, F. Wu, Y. Li, C. Wu, Budding willow branches shaped $Na_3V_2(PO_4)_3$/C nanofibers synthesized via an electrospinning technique and used as cathode material for sodium ion batteries, J. Power Sources 273 (2015) 784–792.

[36] H.X. Liu, Y. Guo, Novel design and preparation of N-doped graphene decorated $Na_3V_2(PO_4)_3$/C composite for sodium-ion batteries, Solid State Ionics 307 (2017) 65–72.

[37] W.H. Yang, W. He, X.D. Zhang, G.H. Yang, J.Y. Ma, Y.Y. Wang, C.L. Wang, $Na_3V_2(PO_4)_3$/N-doped Carbon Nanocomposites with Sandwich Structure for Cheap, Ultrahigh☐Rate, and Long☐Life Sodium☐Ion Batteries, ChemElectroChem 6 (2019) 2020–2028.

[38] J. Yan, T.F.i Lv, L.X. Wang, L. Li , H. Wang, Y. Zhang, F.J. Liu, S.W. Wang, L.Z. Wang, Microwave irradiation preparation of $Na_3V_2(PO_4)_3$@N-doping carbon

cathodes and their lithium ion storage behavior, Solid State Ionics 336 (2019) 67–73.

[39] H. Kim, H. Lim, H.S. Kim, K.J. Kim, D. Byun, W Choi, Polydopamine-derived N-doped carbon-wrapped $Na_3V_2(PO_4)_3$ cathode with superior rate capability and cycling stability for sodium-ion batteries, Nano Research, 12 (2019) 397–404.

[40] H. Wu, C.Y. Hou, G.Z. Shen, T. Liu, Y.L. Shao, R. Xiao, H.Z. Wang, MoS_2/C/C nanofiber with double-layer carbon coating for high cycling stability and rate capability in lithium-ion batteries, Nano Research 11 (2018) 5866–5878.

[41] H.B. Huang, S.H. Luo, C.L. Liu, Y. Yang, Y.C. Zhai, L.J. Chang, M.Q. Li, Double-carbon coated $Na_3V_2(PO_4)_3$ as a superior cathode material for Na-ion batteries, Appl. Surf. Sci. 487 (2019) 1159–1166.

[42] W. Shen, H. Li, Z.Y. Guo, C. Wang, Z.H. Li, Q.J. Xu, H.M. Liu, Y.G. Wang, Y.Y. Xia, Double-Nanocarbon Synergistically Modified $Na_3V_2(PO_4)_3$: An Advanced Cathode for High-Rate and Long-Life Sodium-Ion Batteries, ACS Appl. Mater. Interfaces 8 (2016) 15341–15351.

[43] X.D. Zhang, Z.Y. Bi, G.G. Xu, C.G. Li, W. He, J.F. Zhu, Binary superlattice ceramic membrane-coated soft carbon/hard carbon microspheres for high energy mixed-ion batteries, J. Power Sources, 438 (2019) 226980.

[44] K.L. Zhang, X.D. Zhang, W. He, W.N. Xu, G.G Xu, X.L. Yi, X.N. Yang, J.F. Zhu, Rational design and kinetics study of flexible sodium-ion full batteries based on binder-free composite film electrodes, J. Mater. Chem. A 7 (2019) 9890–9902.

[45] Y.Y. Wang, W.H. Yang, X.D. Zhang, W. He, C.L. Wei, X.L. Yi, Z.Y. Wang, Q.H.

Cheng, J.Y. Ma, High-performance multiphase $Li_{2.5}Na_{0.5}V_2(PO_4)_3$ nanocomposite cathode enabled by hierarchical porous structure, J. Alloy. Compd. 777 (2019) 784–794.

[46] X.L. Yi, W. He, X.D. Zhang, G.H. Yang, Y.Y. Wang, Hollow mesoporous MnO/MnS/SiC/S-CN composites prepared from soda pulping black liquor for lithium-ion batteries, J. Alloy. Compd. 735 (2019) 1306–1313.

[47] X.R. Han, F. Liao, Y.f, Zhang, X.h. Han, C.j. Xu, H.Y. Chen, Solvothermal preparation of zinc cobaltite mesoporous microspheres for high-performance electrochemical supercapacitors, J. Alloy. Compd. 781 (2019) 425–432.

[48] H.Y, Chen, J.P. Wang, F. Liao, X.R. Han, Y.F. Zhang, C.J. Xu, L. Gao, Uniform and porous Mn-doped Co_3O_4 microspheres: Solvothermal synthesis and their superior supercapacitor performances, Ceramics International 45 (2019) 11876–11882.

[49] Z. Wang, C.Y. Yang, T.Q. Lin, H. Yin, P. Chen, D.Y. Wan, F.F. Xu, F.Q. Huang, J.H. Lin, X.M. Xie, M.H. Jiang, H-Doped Black Titania with Very High Solar Absorption and Excellent Photocatalysis Enhanced by Localized Surface Plasmon Resonance, Adv. Funct. Mater., 23 (2013) 5444–5450.

[50] F. Xie, Z. Xu, A.C.S. Jensen, H. Au, Y.X. Lu, V.A. Peters, A.J. Drew, Y.S. Hu, M.M. Titirici, Hard–Soft Carbon Composite Anodes with Synergistic Sodium Storage Performance, Adv. Funct. Mater. 29 (2019) 1901072.

[51] Z.Y. Wang, W. He, X.D. Zhang, Y.Z. Yue, J.H. Liu, C.J. Zhang, L.Y. Fang, Multilevel structures of $Li_3V_2(PO_4)_3$/phosphorus-doped carbon nanocomposites

derived from hybrid V-MOFs for long-life and cheap lithium ion battery cathodes, J. Power Sources 366 (2017) 9–17.

[52] Z.Z. Yan, W. He, X.D. Zhang, X.N. Yang, Y.Y. Wang, X. Zhang, Y.X. Lou, G.G. Xu, N-doped hard carbon ultrathin film-coated $Fe_{1-x}S$ nanoparticles with multi-morphologies for cheap Li ion battery anodes, J. Mater. Sci.: Mater. Electron. 30 (2019) 4527–4540.

[53] C. Liu, N. Xiao, H.J. Li, Nitrogen-Doped soft carbon frameworks built of well-interconnected nanocapsules enabling a superior potassium-ion batteries anode, Chem. Eng. J. (2019) 121759.

[54] L. Chen, Y.M. Zhao, S.H. Liu, Hard carbon wrapped $Na_3V_2(PO_4)_3$@C porous composite extending cycling lifespan for sodium-ion batteries, ACS Appl. Mater. Interfaces (2017) 9 44485–44493.

[55] X. Jiang, L.Q. Yang, B. Ding, B.H. Qu, G Ji, J.Y. Lee, Extending the cycle life of $Na_3V_2(PO_4)_3$ cathodes in sodium-ion batteries through interdigitated carbon scaffolding, J. Mater. Chem. A 4 (2016) 14669–14674.

[56] P.Y. Feng, W. Wang, K.L. Wang, S.J. Cheng, K. Jiang, $Na_3V_2(PO_4)_3$/C synthesized by a facile solid-phase method assisted with agarose as a highperformance cathode for sodium-ion batteries, J. Mater. Chem. A 5 (2017) 10261–10268.

[57] J.L. Liu, J. Wang, C.H. Xu, H. Jiang, C.Z. Li, L.L. Zhang, J.Y. Lin, Z.X. Shen, Advanced Energy Storage Devices: Basic Principles, Analytical Methods, and Rational Materials Design Adv. Sci. 5 (2018) 1700322.

[58] X.B. Zhu, D. Sun, B. Luo, Y. Hu, L. Wang, A stable high-power $Na_2Ti_3O_7/LiNi_{0.5}Mn_{1.5}O_4$ Li-ion hybrid energy storage device, Electrochim. Acta 284 (2018) 30–37.

[59] X. Wang, S. Kajiyama, H. Iinuma, E. Hosono, S. Oro, I. Moriguchi, M. Okubo, A. Yamada, Pseudocapacitance of MXene nanosheets for high-power sodium-ion hybrid capacitors, Nat. Commun. 6 (2015) 6544.

[60] L. Wu, D. Buchholz, D. Bresser, L.G. Chagas, S. Passerini, Anatase TiO_2 nanoparticles for high power sodium-ion anodes, J. Power Sources 251 (2014) 379–385.

Acknowledgements

Additional information

Supplementary Information accompanies this paper at http://www

Competing financial interests: The authors declare no competing financial interests.

Corresponding author line Correspondence and requests for materials should be addressed to X.Z. (email: zxd1080@126.com), to W.H. (email: hewen1960@126.com, or to J.Z. (email: jiefang.zhu@kemi.uu.se)

1

2 **Fig. 1.** (a-c) SEM images of the pecursor sample after solvothermal treatment at

3 different magnifications. (d-g) A schematic diagram of the formation process for

4 N-HSDC/NVP-HMs, (d) structural representations of ethylene glycol (EG) and

5 ethylenediamine (EN), (e) self-assembly of EG and EN with some kinds of ions, (f)

6 structure model of the precursor of N-HSDC/NVP-HMs after solvothermal treatment,

7 (g) structure model of N-HSDC/NVP-HMs after calcinations. (hi) Inner structure

8 models of a N-HSDC/NVP-HM. (j-l) SEM images of N-HSDC/NVP-HMs-1(j),

9 N-HSDC/NVP-HMs-2 (k) and N-HSDC/NVP-HMs-3 (l).

10

11 **Fig. 2.** Structure and chemical state characterizations of different samples. (a) X-ray

12 diffraction patterns of different samples. (b-d) Particle size distribution curves of the

13 different samples. (e) The Nitrogen adsorption/desorption isotherms of different

14 samples and their corresponding pore-size distribution curves (f). (g) The Raman

15 spectrum of N-HSDC/NVP-HMs-2 sample is deconvoluted by three Gaussian peaks.

16 (h) XPS survey spectrum of N-HSDC/NVP-HMs-2 sample and high resolution XPS

17 spectra of C1s (i) and N1s (j) with N-doped carbon schematic inset.

18

19

20 **Fig. 3.** Microscopic structure and element compositional analysis of

21 N-HSDC/NVP-HMs-2. TEM image (a) and HRTEM images (bc) of

22 N-HSDC/NVP-HMs-2. (d) EDX mapping area of a single N-HSDC/NVP-HM and

1 corresponding elemental distribution mappings of nitrogen (e), carbon (f), oxygen (g),

2 phosphorus (h), vanadium (i) and sodium (j).

3

4 **Fig. 4** Schematic illustration of Na-ion storage and diffusion in N-doped soft carbon,

5 N-doped hard carbon and N-doped hard/soft double carbon.

6

7 **Fig. 5.** Electrochemical property comparison of different cathodes synthesized with

8 different amount of EG/EN mixed solution in SIBs. (a) The initial charge-discharge

9 curves of different cathodes in the voltage range of 2.0–4.0 V at 10 C. (b) The CV

10 curves of different cathodes at the scan rate of 0.1 mV s^{-1}. (c) The Nyquist plots of

11 different cathodes before cycling for the frequencies ranging from 10 Hz to 100 kHz

12 during the discharge state. Rate capability comparison (d) and energy density

13 comparison (e) of different cathodes at different rates. (f) Ragone plots (energy

14 density vs. power density) of different cathodes. (g) Capacity retentions of different

15 cathodes for 1000 cycles at 10 C.

16

17 **Fig. 6.** Electrochemical property comparison of N-HSDC/NVP-HMs-2, NVP/C and

18 NVP cathodes in SIBs. (a) The initial charge-discharge curves of different cathodes in

19 the voltage range of 2.0–4.0 V at 0.5 C. Rate capability comparison (b) and energy

20 density comparison (c) of three samples at different rates. (d) The initial

21 charge-discharge curves of N-HSDC/NVP-HMs-2 in the wide voltage range of 0.5–

22 4.5 V at different rates. (e) The CV curves of different cathodes at the scan rate of 0.1

1   mV s^{-1}. (f) The Nyquist plots of different cathodes before cycling for the frequencies

2   ranging from 10 Hz to 100 kHz during the discharge state. (g) Long-term cycling

3   performance of the N-HSDC/NVP-HMs-2 at a current rate of 10 C over 8898 cycles.

4   (h) Cycling performance of the N-HSDC/NVP-HMs-2 at a high current rate of 20 C
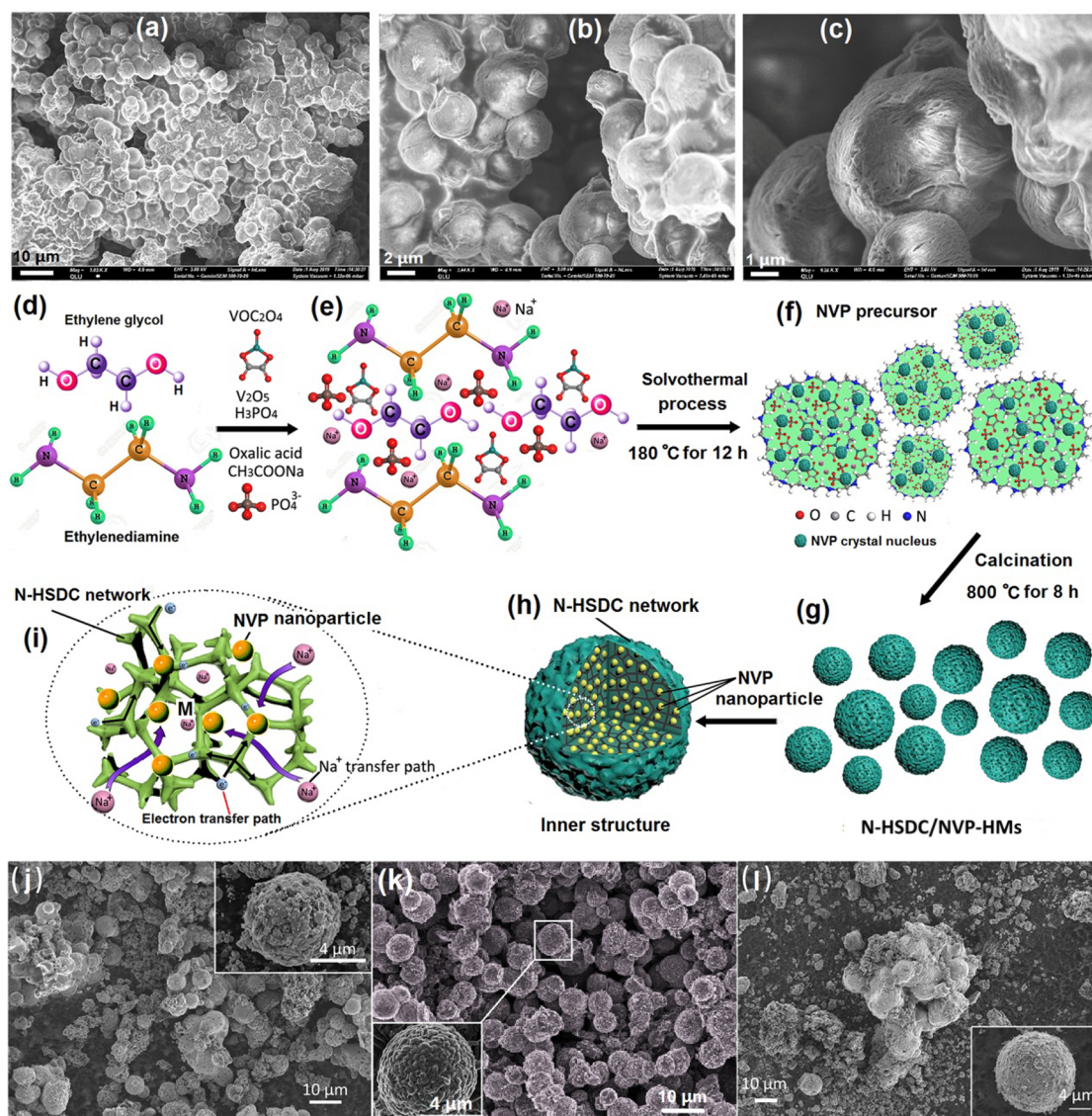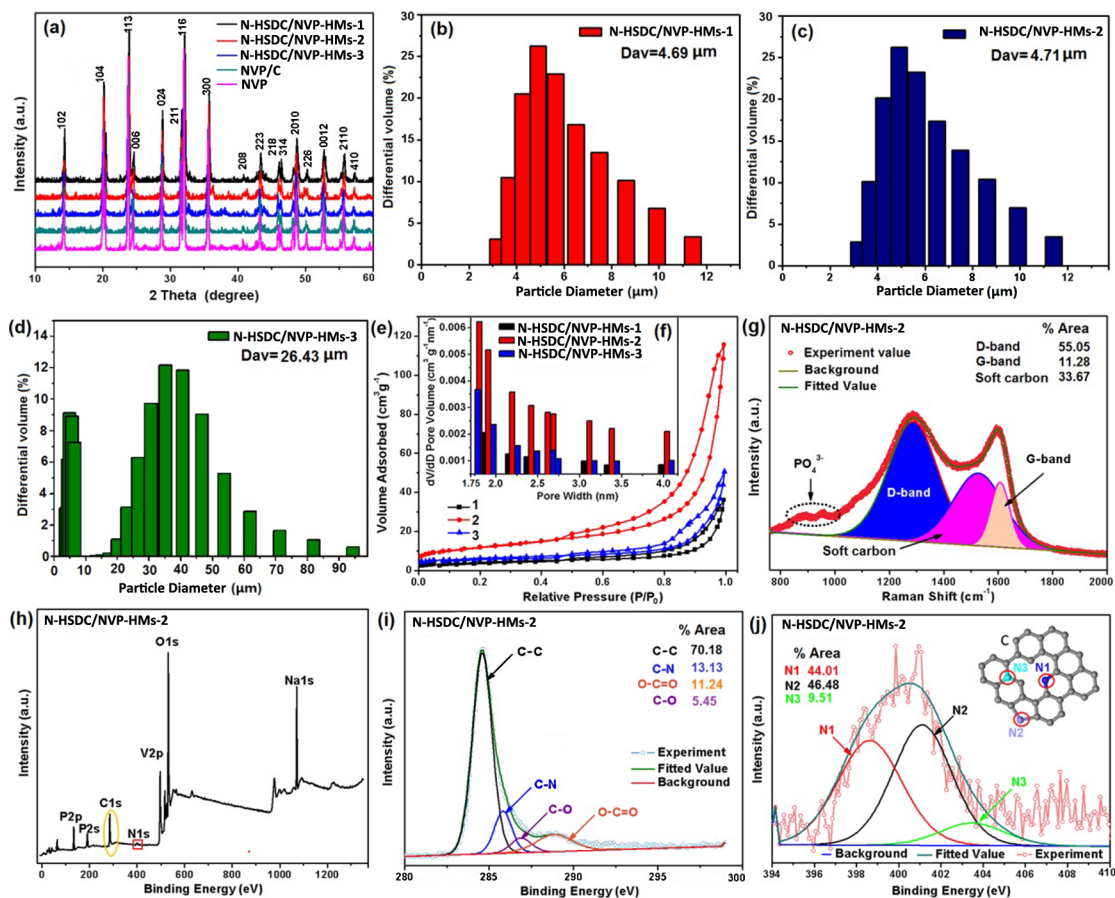
5   over 600 cycles.

6

7   **Fig. 7.** (a) CV curves of N-HSDC/NVP-HMs-2 at sweep rates from 0.2 to 0.5 mV s^{-1}

8   between 0.5 and 4.5 V. (b) Determination of b-value using the relationship between

9   peak current and sweep rates. (c) Diagram of capacitive contribution (the red zone) to

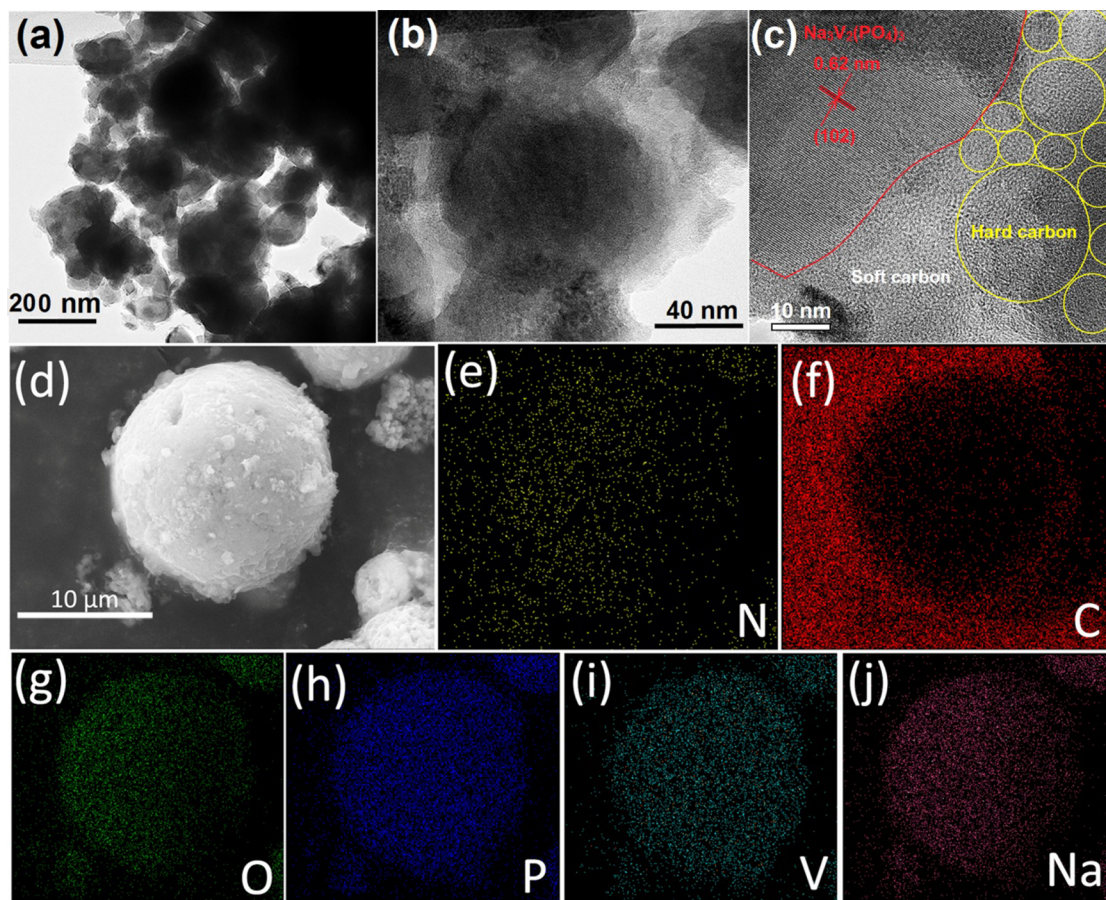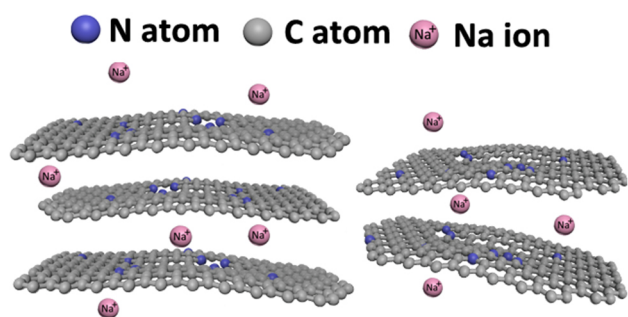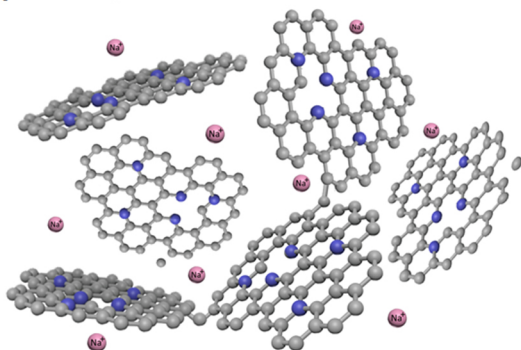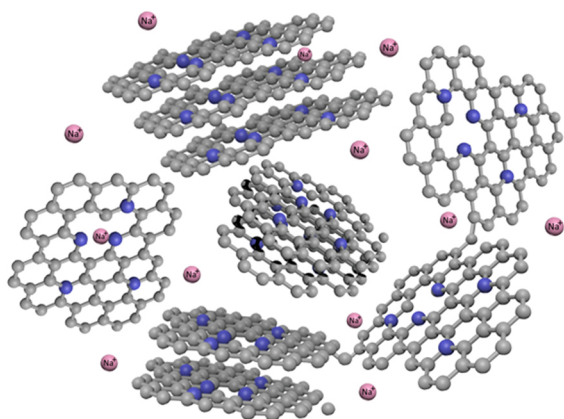10   the total capacity at different sweep rates.

11

12   **Fig. 8**. Schematic diagrams of the reaction mechanism for the "pseudocapacitive

13   behaviour" of Na^{+} storage in N-HSDC/NVP-HMs.

14
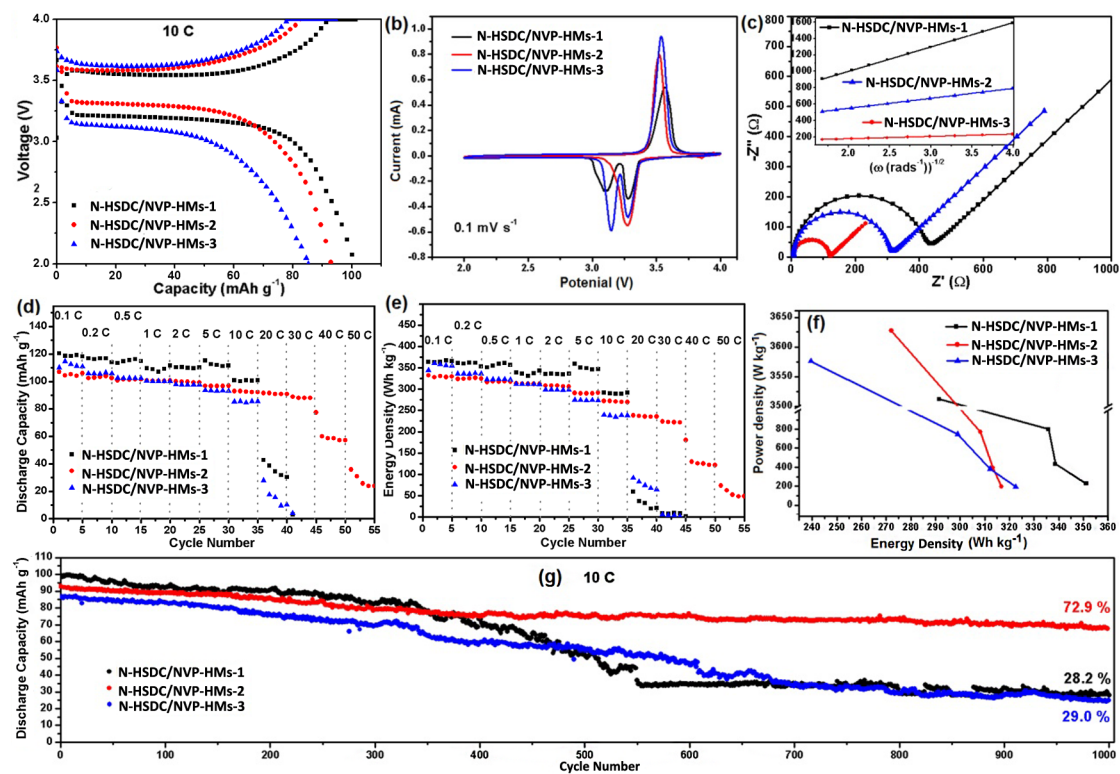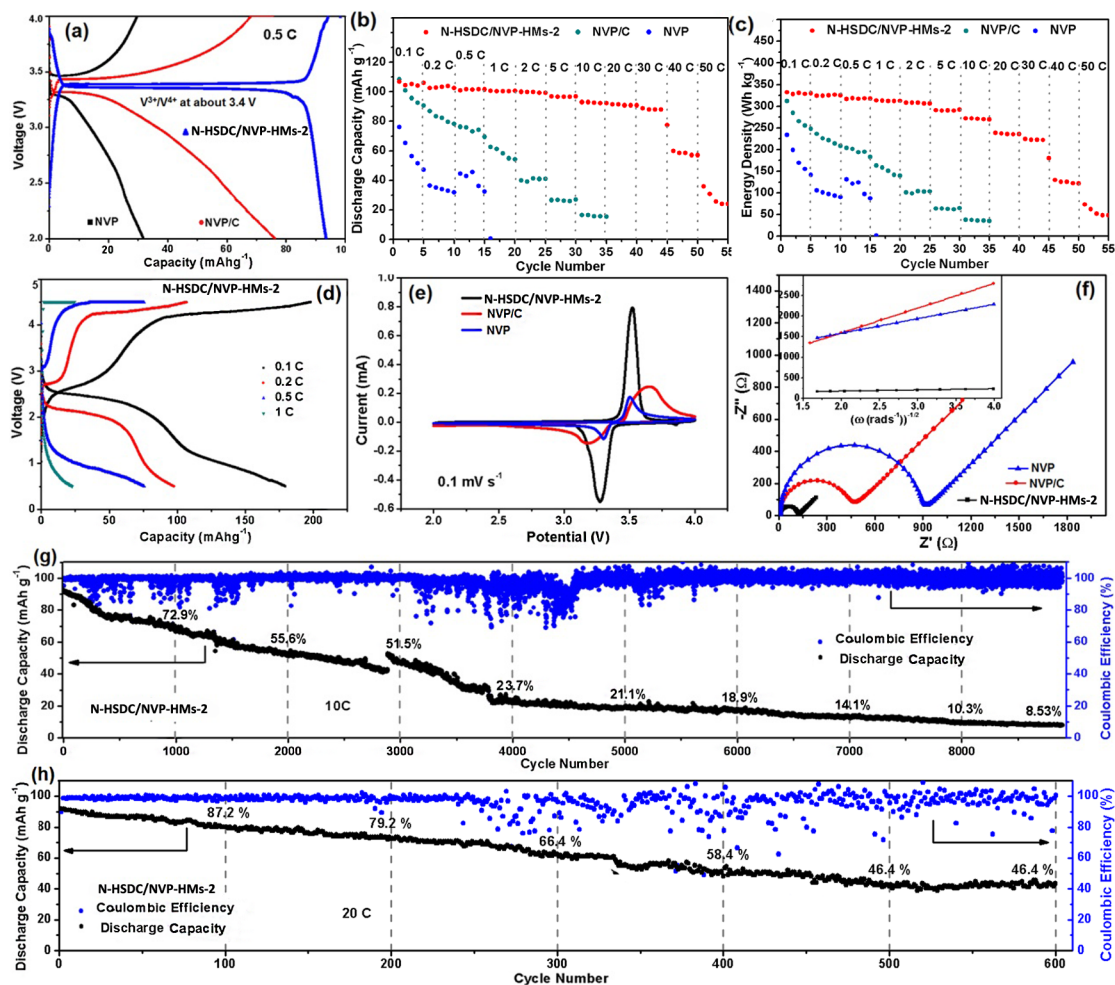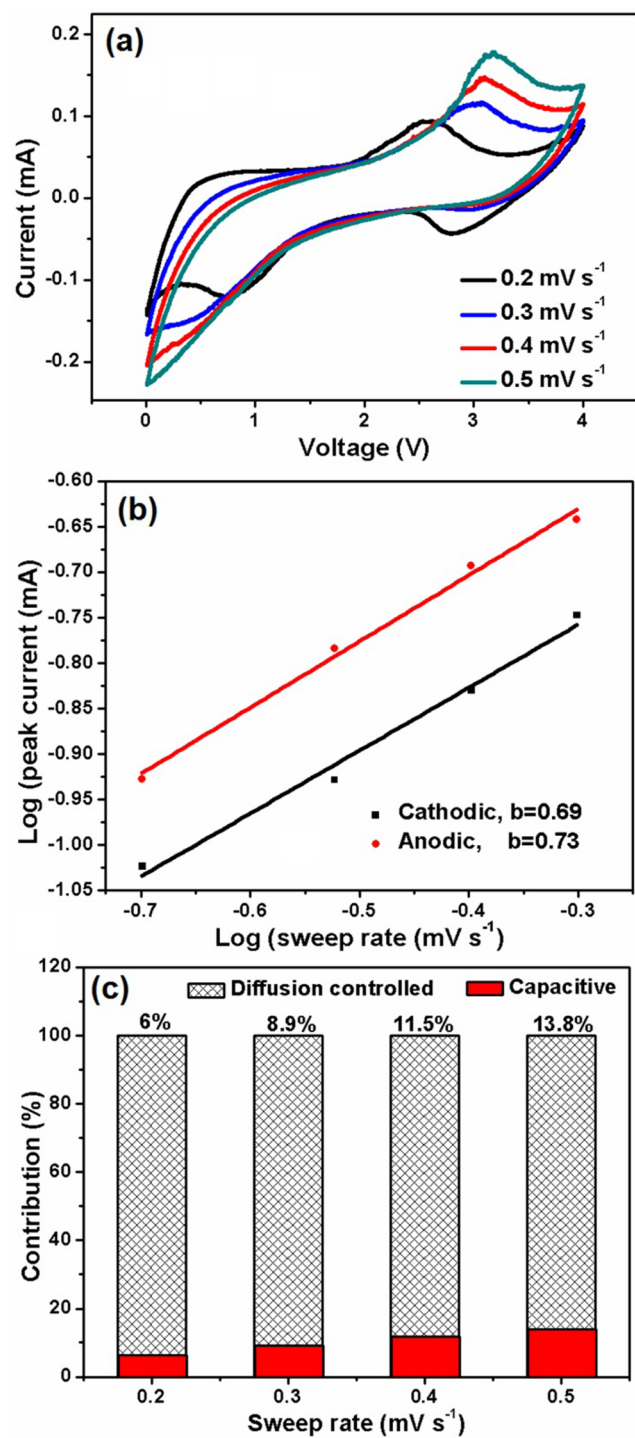
(a) N-HSDC/NVP-HMs-1, N-HSDC/NVP-HMs-2, N-HSDC/NVP-HMs-3, NVP/C, NVP

(b) N-HSDC/NVP-HMs-1, Dav=4.69 μm

(c) N-HSDC/NVP-HMs-2, Dav=4.71 μm

(d) N-HSDC/NVP-HMs-3, Dav= 26.43 μm

(e) N-HSDC/NVP-HMs-1, N-HSDC/NVP-HMs-2, N-HSDC/NVP-HMs-3

(f)

(g) N-HSDC/NVP-HMs-2, Experiment value, Background, Fitted Value, % Area: D-band 55.05, G-band 11.28, Soft carbon 33.67, PO_4^{3-}, D-band, G-band, Soft carbon

(h) N-HSDC/NVP-HMs-2, O1s, Na1s, V2p, C1s, P2p, P2s, N1s

(i) N-HSDC/NVP-HMs-2, % Area: C-C 70.18, C-N 13.13, O-C=O 11.24, C-O 5.45, Experiment, Fitted Value, Background

(j) N-HSDC/NVP-HMs-2, % Area: N1 44.01, N2 46.48, N3 9.51, Background, Fitted Value, Experiment

(a) 200 nm

(b) 40 nm

(c) Na₃V₂(PO₄)₃ 0.62 nm (102) Soft carbon Hard carbon 10 nm

(d) 10 μm

(e) N

(f) C

(g) O

(h) P

(i) V

(j) Na

(a) N-doped soft caibon

🔵 **N atom** ⚪ **C atom** 🔴 **Na ion**
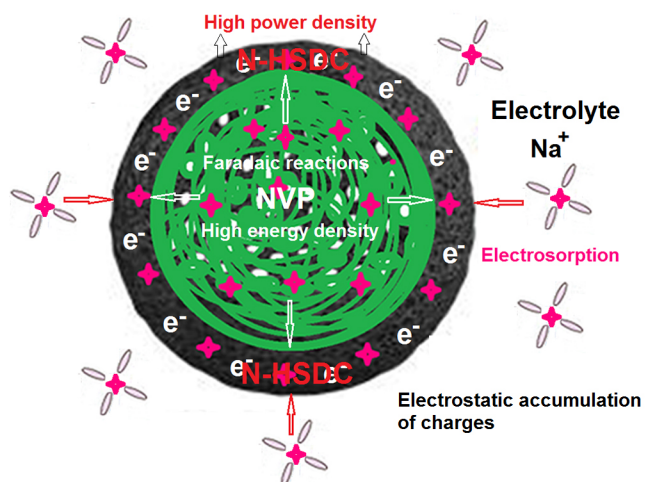
(b) N-doped hard carbon

(c) N-doped hard/soft double-carbon

(a) Battery behaviour of NVP and pseudocapacitive behaviour of N-HSDC combined in N-HSDC/NVP-HMs

High power density

N-HSDC

e⁻

Faradaic reactions

NVP

High energy density

Electrolyte Na⁺

Electrosorption

N-HSDC

Electrostatic accumulation of charges

(b) N-HSDC/NVP-HMs

Na metal

Cathode   Electrolyte   Anode

Current Collector

e⁻

Na⁺

Separator
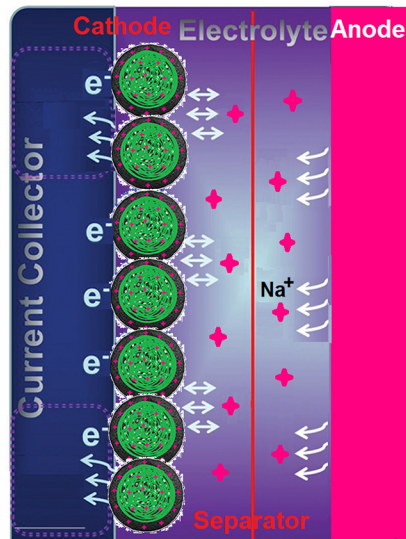
Highlights

► N-doped hard/soft double-carbon-coated $Na_3V_2(PO_4)_3$ hybrid-porous microspheres

were synthesized.

► The EN/EG mixed solution controlled the formation of the hybrid-porous

microspheres.

► The microsphere cathode shows superior rate capability and high energy density.

►It also exhibits ultrahigh power density due to pseudocapacitive behavior.

Declaration of interests

v☐v The authors declare that they have no known competing financial interests or personal relationships that could have appeared to influence the work reported in this paper.

☐The authors declare the following financial interests/personal relationships which may be considered as potential competing interests: